DOI 10.1007/s11106-021-00222-4
Powder Metallurgy and Metal Ceramics, Vol. 60, Nos. 3-4, July, 2021 (Russian Original Vol. 60, Nos. 3-4, March-April, 2021)

THEORY, MANUFACTURING TECHNOLOGY, AND PROPERTIES OF POWDERS AND FIBERS

THE INFLUENCE OF THE ZrO_2 SOLID SOLUTION AMOUNT ON THE PHYSICOCHEMICAL PROPERTIES OF Al_2O_3–ZrO_2–Y_2O_3–CeO_2 POWDERS

M.Yu. Smyrnova-Zamkova,[1,3] O.K. Ruban,[1] O.I. Bykov,[1] M.Ya. Holovchuk,[2] T.V. Mosina,[1] O.I. Khomenko,[1] and E.V. Dudnik[1]

UDC 541.1.621.762

Alumina-based nanocrystalline powders with different ZrO_2 amounts were produced for the first time by hydrothermal synthesis in an alkaline environment for designing zirconia toughened alumina (ZTA) composites. In ZTA composites, ZrO_2 solid solution particles codoped with ceria and yttria are distributed in a rigid Al_2O_3 matrix. To examine the physicochemical properties, 90 wt.% Al_2O_3–10 wt.% ZrO_2 (Y_2O_3, CeO_2) and 58.5 wt.% Al_2O_3–42.5 wt.% ZrO_2 (Y_2O_3, CeO_2) powders were used. The ZrO_2 solid solution had composition 90 mol.% ZrO_2–2 mol.% Y_2O_3–8 mol.% CeO_2. The hydrothermal powders were heat treated in the temperature range 400–1450°C and examined by X-ray diffraction, differential thermal analysis, and electron microscopy. The powder specific surface area was determined by the BET method. The sizes of primary particles were determined with the Scherrer equation. The AMIC software (Automatic Microstructure Analyzer) was employed to process the morphology analysis results. The phase transformations and active sintering of the ZTA powders determined the dependences showing the sizes of primary particles and the specific surface area of the powders versus the heat treatment temperature. With higher ZrO_2 content, temperature of the F-ZrO_2 → T-ZrO_2 phase transformation decreased, the likelihood of M-ZrO_2 to emerge increased, and the sequence of Al_2O_3 phase transformations changed after the boehmite had decomposed. The variation in the morphology and specific surface area of the powders in the heat treatment process indicated that their sintering activity increased. The dependence of the shape factor characterizing the nanocrystalline 90AZG and 58.5AZG powders on the heat treatment temperature was studied. The starting nanosized 90AZG and 58.5AZG powders had a similar distribution of agglomerates according to the shape factor. Round agglomerates and multifaceted regular agglomerates were predominant. The way in which the shape factor of the agglomerates varied with temperature was associated with a topochemical memory effect manifested by the powders. The mechanical properties of the samples sintered from the hydrothermal nanocrystalline

[1]Frantsevich Institute for Problems of Materials Science, National Academy of Sciences of Ukraine, Kyiv, Ukraine. [2]Karpenko Physicomechanical Institute, National Academy of Sciences of Ukraine, Lviv, Ukraine.
[3]To whom correspondence should be addressed; e-mail: smirnovazamkova@ukr.net.

Translated from Poroshkova Metallurgiya, Vol. 60, Nos. 3–4 (538), pp. 3–17, 2021. Original article submitted January 25, 2021.

90AZG and 58.5AZG powders were examined. With increasing ZrO_2 content, the microhardness of the ZTA composites decreased from 195 to 160 MPa, fracture toughness (K_{Ic}) increased from 6 to 8 MPa · $m^{0.5}$, and Vickers hardness decreased from 8.3 to 5.6 GPa. The improvement in consolidation methods for ZTA composites will allow tool, structural, and functional ceramics with the required properties to be produced.

Keywords: *Al_2O_3–ZrO_2 (Y_2O_3, CeO_2) system, ZTA composites, hydrothermal synthesis in alkaline environment, nanocrystalline powder, shape factor, ZrO_2 solid solution.*

INTRODUCTION

Composites with an Al_2O_3 matrix strengthened with ZrO_2 particles, termed zirconia toughened alumina (ZTA) composites, combine high hardness of the Al_2O_3 matrix and high fracture toughness of the ZrO_2 reinforcement phase. The mechanical properties of ZTA composites depend on the amount of a ZrO_2 metastable tetragonal solid solution (T-ZrO_2) or monoclinic ZrO_2 solid solution (M-ZrO_2) in the Al_2O_3 matrix and on the sizes of Al_2O_3 and ZrO_2 particles. The fracture toughness of these materials reaches 17 MPa · $m^{0.5}$ and the bending strength 1700 MPa. The high strength of ZTA composites is due to several strengthening mechanisms: transformation hardening, crack deflection/branching, microcracking, and modular load transfer [1].

Zirconia toughened alumina composites were previously used to make grinding and metal cutting tools [2–4]. In recent times, ZTA ceramics have attracted attention for their excellent high-temperature mechanical strength, high oxidation resistance, heat resistance, and wear resistance, low thermal conductivity, and insignificant thermal expansion mismatch between ZTA ceramics and metals. High-strength materials, such as blades for cutting tools, insulators for electrosurgical operations, valve seals, body armor, pump components, oxygen sensors, molds, etc., were made from ZTA ceramics [5–7]. To increase the viscosity of light ceramic armor, found to be effective in counteracting high-velocity and armor-piercing projectiles and withstanding a large number of impacts, ZTA composites that contain 10–20 wt.% ZrO_2 stabilized by Y_2O_3 are promising [8].

The replacement of Al_2O_3 (BIOLOX® Forte) by ZTA (BIOLOX® Delta) in bioinert orthopedic and dental implants allowed more complex articles to be produced and the percentage of fractures in prosthetic hip joint heads to be reduced significantly (from 0.02 to 0.002%). For this reason, ZTA composites are called the gold standard for ceramic hip joints in medicine [9].

The main ways for improvement of ZTA composites are to increase their strength, fracture toughness, and resistance to low-temperature degradation (ageing). Noteworthy is that a great number of research papers focus on ceria doping of ZTA composites with an Y_2O_3-stabilized ZrO_2 solid solution [10–12]. To stabilize T-ZrO_2 in such ZTA composites, a maximum of 25 wt.% CeO_2 is required. Ceria doping of ZTA composites that do not contain Y_2O_3 in ZrO_2 solid solutions is not addressed in the literature [13–15].

Interest in ZTA composites with increased ZrO_2 content has been growing recently. Thus, ZTA ceramics containing up to 30 wt.% ZrO_2 are regarded as promising materials for operation at cryogenic temperatures [16], and ZTA ceramics of eutectic composition (42.8 wt.% ZrO_2(Y_2O_3)–57.2 wt.% α-Al_2O_3) can be effective for high-temperature applications [17] and for deposition of ceramic topcoat layers of thermal barrier coatings [18, 19]. The 50 wt.% Al_2O_3–50 wt.% ZrO_2 ($8Y_2O_3$) composite shows an optimal combination of mechanical properties (σ_{bend} within 1000 MPa and average hardness approximately 18 GPa) [20]. The paper [21] examines how additions of superfine eutectic 50 wt.% Al_2O_3–42 wt.% ZrO_2–8 wt.% Y_2O_3 powder (in terms of pure oxides) influence the density and microstructure of corundum ceramics to improve the properties of integrated circuit substrates.

Analysis of current research efforts intended to improve the properties of ZTA composites indicates that Y_2O_3 remains the most popular stabilizer for T-ZrO_2 [7]. At the same time, data on the effect exerted by the doping of ZTA composites by ceria introduced mechanically demonstrate that the mechanical properties of ZTA composites can be improved to the extent maximum when CeO_2 is present in the ZrO_2 solid solution [22–24].

Additions of CeO_2 stabilize the metastable T-ZrO_2 solid solution and slow down the T-ZrO_2 → M-ZrO_2 phase transition [25, 26].

There are virtually no studies focusing on ZTA composites with ZrO_2 being stabilized by both yttrium and cerium oxides. Hence, of interest is to study such ZTA composites since they afford materials that consist of a rigid Al_2O_3 matrix with ZrO_2 solid solution particles being distributed in it and possess adequate fracture toughness.

Our objective is to examine the physicochemical and mechanical properties of nanocrystalline Al_2O_3-based powders in the Al_2O_3–ZrO_2–Y_2O_3–CeO_2 system produced by hydrothermal synthesis in an alkaline environment depending on the content of ZrO_2 solid solution.

For experiments, we chose the following powders: 90 wt.% Al_2O_3–10 wt.% ZrO_2 (Y_2O_3, CeO_2) → 90 wt.% AZG and 58.5 wt.% Al_2O_3–42.5 wt.% ZrO_2 (Y_2O_3, CeO_2) → 58.5 wt.% AZG. The ZrO_2 solid solution had the following composition: 90 mol.% ZrO_2–2 mol.% Y_2O_3–8 mol.% CeO_2.

EXPERIMENTAL PROCEDURE

Hydrothermal synthesis methods afford high-quality pure powders of varying composition with controlled particle sizes and high sintering activity [27]. The starting nanocrystalline ZTA powders, 90AZG and 58.5AZG, were prepared by hydrothermal synthesis in an alkaline environment. The starting substances were zirconium oxychloride $ZrOCl_2 \cdot 8H_2O$, yttrium nitrate $Y(NO_3)_3 \cdot 6H_2O$, cerium nitrate $Ce(NO_3)_3 \cdot 6H_2O$, and aluminum nitrate $Al(NO_3)_3$ [28].

To study the physicochemical properties of loose nanocrystalline Al_2O_3–ZrO_2–Y_2O_3–CeO_2 powders, they were heat treated in air in the range 400–1450°C (in 150°C steps, with holding for 2 h at each temperature). The properties of the nanosized powders following hydrothermal synthesis and of the nanocrystalline powders following heat treatment were examined by X-ray diffraction (XRD) (DRON-1.5, Cu-K_α radiation, 1–4°/min scan rate, 2θ = 10–90°), differential thermal analysis (Q-1500 D derivative thermographic analyzer, 10°C/min heating rate in the range 20–1000°C), and electron microscopy (scanning electron microscope with a REM 106I energy-dispersive microanalyzer). Thermal nitrogen adsorption/desorption (BET method) was employed to determine the specific surface area of the powders. The sizes of primary particles were calculated with the Scherrer equation. To process the morphology analysis results, we used the AMIC software (Automatic Microstructure Analyzer). The microhardness was measured by a Falkon 509 hardness tester (Netherlands) with an indenter load being 300 N (30 kg).

RESULTS AND DISCUSSION

X-ray diffraction (XRD) data indicate that hydrothermal synthesis resulted in a mixture of boehmite (AlO(OH)) and a low-temperature metastable cubic ZrO_2-based fluorite-type solid solution (F-ZrO_2). The specific surface area of the starting powders was 127 m^2/g (90AZG) and 71 m^2/g (58.5AZG).

The DTA curve for the 90AZG powder (Fig. 1*a*) shows two wide endothermic effects in the ranges 20–220°C and 400–530°C, which are seen as minima on the DTG curve. This testifies that the sample loses its weight intensively. A wide endothermic effect in the range 20–220°C with a minimum at 100°C (weight loss within 12%) corresponds to the removal of adsorbed moisture and partial dehydroxylation of boehmite. Subsequent exothermic effects with maxima at 220 and 250°C (Fig. 1*a*) are shown by insignificant oscillations on the DTG curve. The TG curve indicates that the sample weight loss is within 1%. The above exothermic effects correspond to the crystallization of amorphous ZrO_2 left after hydrothermal synthesis and to the partial crystallization of boehmite.

Residual amorphous $Zr(OH)_4$ transforms to ZrO_2 as follows [28]:

$$Zr(OH)_4 = ZrO_{1.5}(OH) + 1.5H_2O, \quad (1)$$

$$ZrO_{1.5}(OH) = ZrO_2 + 0.5H_2O. \quad (2)$$

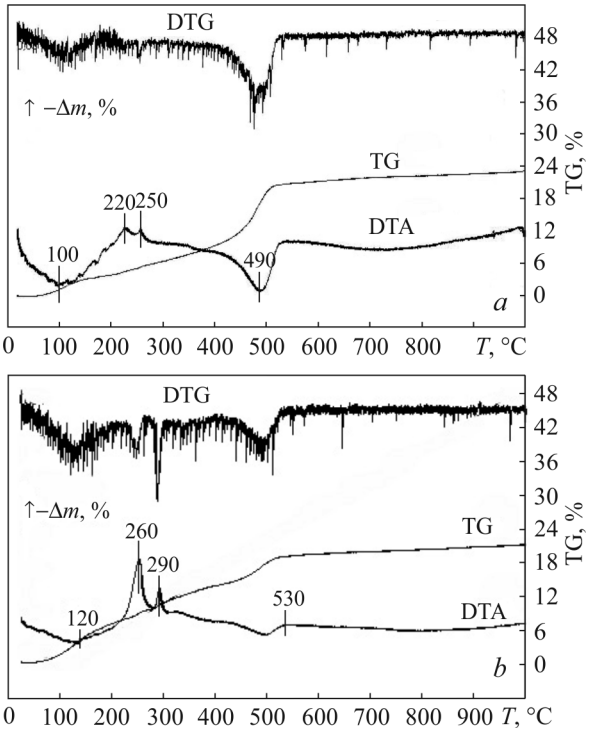

Fig. 1. Differential thermal analysis data for the nanosized 90AZG (*a*) and 58.5AZG (*b*) powders

The endothermic effects in the range 400–530°C with a minimum at 490°C can probably be attributed to the removal of residual coordinately bound moisture (OH^- groups) and to the final decomposition of boehmite by reaction

$$2AlO(OH) = Al_2O_3 + H_2O. \quad (3)$$

This agrees with stoichiometric calculations indicating that the weight loss is 15%, while the TG curve for the 90AZG sample (Fig. 1*a*) shows 12%.

The derivative thermogravimetric patterns for the nanosized 58.5AZG (Fig. 1*b*) and 90AZG powders mainly differ by the intensity of effects on the DTA curve. One endothermic effect in the range 20–180°C with a minimum at 120°C (Fig. 1*b*) corresponds to intensive weight loss (approximately 6%). With greater content of the ZrO_2 solid solution, the exothermic maxima become clearer and sharper (Fig. 1*b*). The two exothermic effects on the DTA curve for the nanosized 58.5AZG powder with maxima at 260 and 290°C (Fig. 1*b*) are manifested as two sharp minima on the DTG curve, indicating that the sample loses weight rapidly. The exothermic effects probably denote the crystallization of amorphous ZrO_2 left after hydrothermal synthesis. The other endothermic effect, between 450 and 530°C with a minima at 500°C (Fig. 1*b*), involves approximately 5% weight loss.

Three stages in which hydrothermal powders lose their weight in heat treatment can be singled out. The first stage proceeds in the range 20–150°C, the second stage, corresponding to a significant weight loss of the samples, takes place in the range 180–500°C, and the third stage, when weigh loss is almost no longer observed, occurs in the range 500–1000°C. The TG curves demonstrate that the total weight loss is approximately the same and varies from 20% (Fig. 1*b*) to 23% (Fig. 1*a*) when the samples are heated to 1000°C.

Figure 2 shows SEM data for the nanosized powders following hydrothermal synthesis. Irregular multifaceted agglomerates form in both cases (90AZG and 58.5AZG). They primarily differ by size. The 90AZG powder contains 5–15 μm agglomerates, individual agglomerates reaching 25 μm (Fig. 2*a*), while the 58.5AZG powder has mainly agglomerates varying from 15 to 40 μm in size and also includes 5 μm agglomerates (Fig. 2*b*). The coarse agglomerates in both powders do not seem to be monolithic but consist of agglomerates to 5 μm in size. The agglomerates to 5 μm in size in turn consist of agglomerates to 1 μm (Fig. 2*a*, *b*).

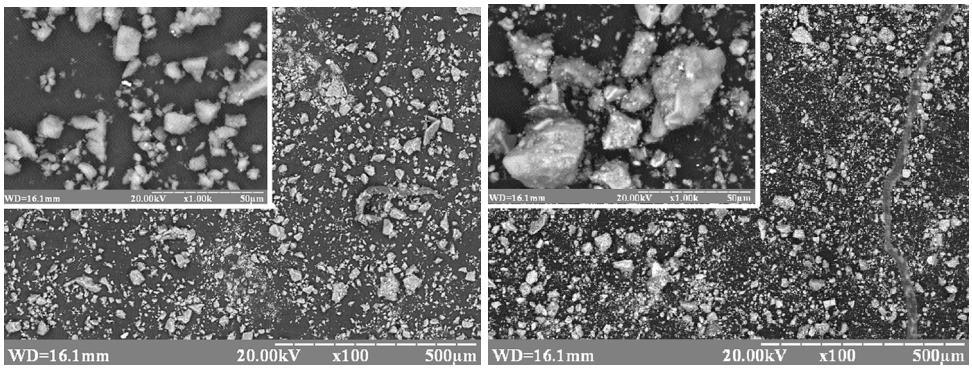

a *b*

Fig. 2. SEM data for the nanosized 90AZG (*a*) and 58.5AZG (*b*) powders following hydrothermal synthesis

The XRD data indicate that heat treatment of the hydrothermal 90AZG and 58.5AZG powders involves the decomposition of boehmite and phase transformations of Al_2O_3 and ZrO_2 (Figs. 3 and 4; Table 1). After being heat treated at 400°C, both powders retain the starting phase composition: two phases are identified in the X-ray diffraction patterns, boehmite and F-ZrO_2 (Fig. 3*a* and Fig. 4*a*). The F-ZrO_2 phase remains in place after the powders are heat treated at 550°C, but the reflection intensity ratios in the X-ray diffraction patterns suggest that

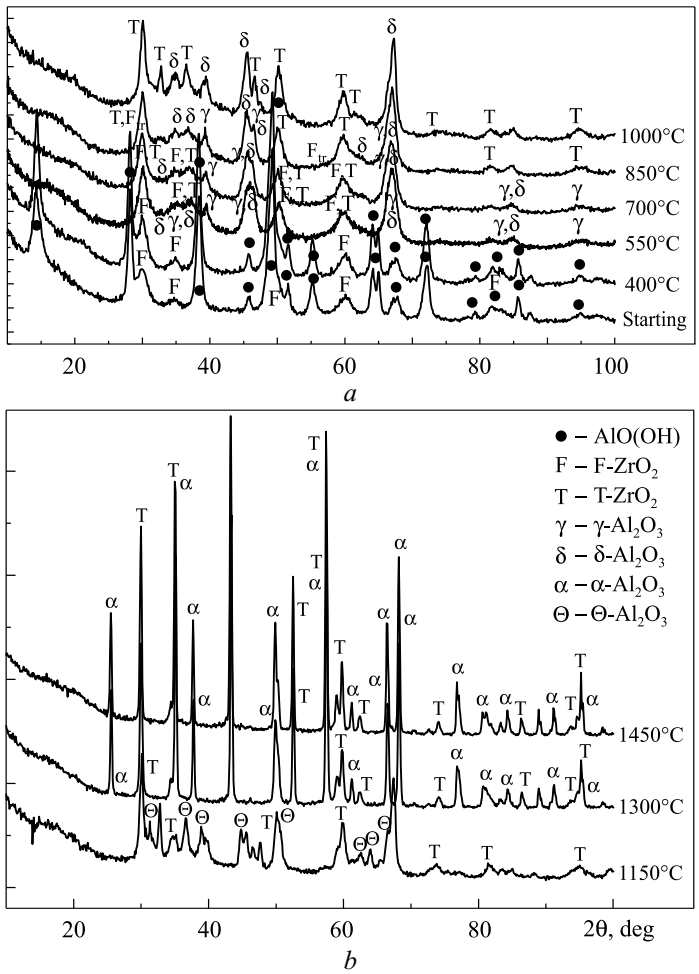

Fig. 3. X-ray diffraction patterns for the 90AZG powder following hydrothermal synthesis and heat treatment in the ranges 400–1000°C (*a*) and 1150–1450°C (*b*)

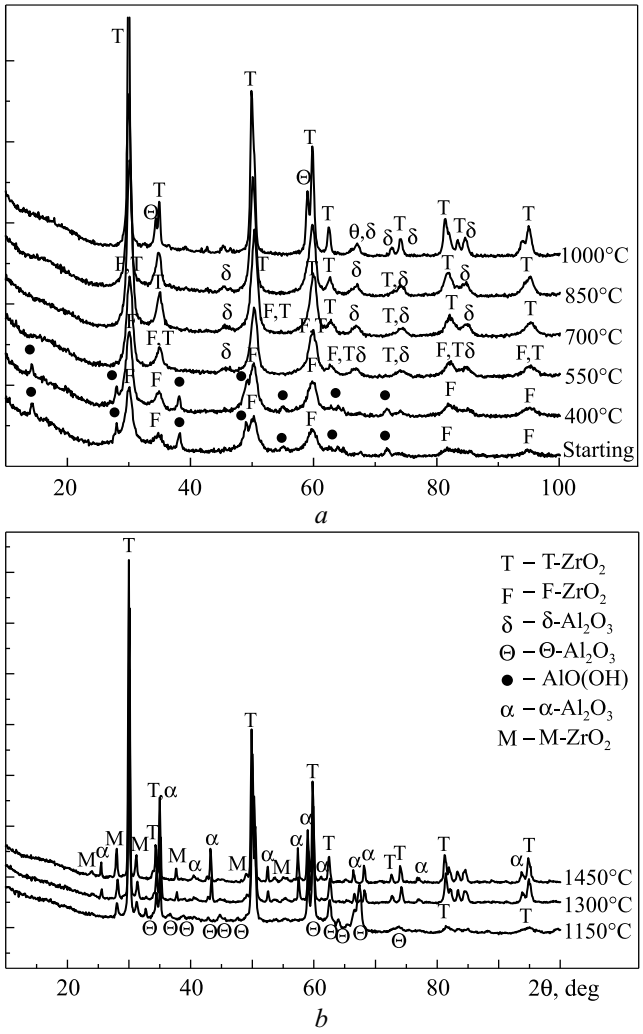

Fig. 4. X-ray diffraction patterns for the 58.5AZG powder following hydrothermal synthesis and heat treatment in the ranges 400–1000°C (*a*) and 1150–1450°C (*b*)

TABLE 1. XRD Data for the 90AZG and 58.5AZG Powders Following Hydrothermal Synthesis and Heat Treatment

Temperature, °C	Powder phase composition	
	90AZG	58.5AZG
Starting hydrothermal powders	F-ZrO_2, boehmite	F-ZrO_2, boehmite
400	F-ZrO_2, boehmite	F-ZrO_2, boehmite
550	F-ZrO_2, T-ZrO_2, γ-Al_2O_3, δ-Al_2O_3 (traces)	F-ZrO_2, T-ZrO_2, δ-Al_2O_3
700	F-ZrO_2, T-ZrO_2, γ-Al_2O_3, δ-Al_2O_3	F-ZrO_2 (traces), T-ZrO_2, δ-Al_2O_3
850	T-ZrO_2, F-ZrO_2 (traces), δ-Al_2O_3, γ-Al_2O_3 (traces)	T-ZrO_2, δ-Al_2O_3
1000	T-ZrO_2, δ-Al_2O_3	T-ZrO_2, δ-Al_2O_3, Θ-Al_2O_3
1150	T-ZrO_2, Θ-Al_2O_3	T-ZrO_2, M-ZrO_2, Θ-Al_2O_3
1300	T-ZrO_2, α-Al_2O_3	T-ZrO_2, M-ZrO_2, α-Al_2O_3
1450	T-ZrO_2, α-Al_2O_3	T-ZrO_2, M-ZrO_2, α-Al_2O_3

T-ZrO_2 traces should be present (Fig. 3*a* and Fig. 4*a*). Boehmite decomposes at 550°C. The γ-Al_2O_3 phase shows up in the 90AZG powder, but the reflection intensity ratio indicates that δ-Al_2O_3 traces might be present (Fig. 3*a*). Contrastingly, only the δ-Al_2O_3 phase forms in the 58.5AZG powder (Fig. 4*a*). Following heating of the hydrothermal nanosized 90AZG and 58.5AZG powders in the range 400–550°C, the endothermic effects on the DTA curves (Fig. 1) correspond not only to the removal of crystalline bound water but to boehmite decomposition.

The F-ZrO_2 → T-ZrO_2 phase transformation proceeds when the 90AZG powder is heat treated at 700°C; moreover, a mixture of γ-Al_2O_3 and δ-Al_2O_3 emerges (Fig. 3*a*, Table 1). In the 58.5AZG powders, the ZrO_2 phase transformation finishes at 700°C and two phases, T-ZrO_2 and δ-Al_2O_3, are identified (Fig. 4*a*). When temperature increases to 850°C, the X-ray diffraction patterns for the nanocrystalline 90AZG powder show reflections of T-ZrO_2 and δ-Al_2O_3, but the reflection intensity ratio suggests that F-ZrO_2 and γ-Al_2O_3 traces might be present (Fig. 3*a*). The phase composition of the 58.5AZG powder remains unchanged (Fig. 4*a*).

The F-ZrO_2 → T-ZrO_2 phase transformation finishes in the 90AZG powder following heat treatment at 1000°C: the X-ray diffraction pattern shows two phases, T-ZrO_2 and δ-Al_2O_3 (Fig. 3*a*). The δ-Al_2O_3 → Θ-Al_2O_3 phase transformation begins and the T-ZrO_2 phase shows up in the 58.5AZG powder (Fig. 4*a*). The Θ-Al_2O_3 phase forms in the 90AZG powder subjected to heat treatment at 1150°C, but δ-Al_2O_3 traces remain as well (Fig. 3*b*). The α-Al_2O_3 phase appears after the nanocrystalline 90AZG powder is heat treated at 1300°C and remains in place after 1450°C (Table 1). Note that the 90AZG powder contains the T-ZrO_2 phase but has no M-ZrO_2 after heat treatment in the range 1000–1450°C (Fig. 3*b*).

The δ-Al_2O_3 → Θ-Al_2O_3 phase transformation in the 58.5AZG powder occurs in the range 1000–1150°C (Fig. 4*a*, *b*), and the Θ-Al_2O_3 → α-Al_2O_3 phase transition is observed at 1300°C (Fig. 4*b*). The T-ZrO_2 phase that finally forms before 850°C remains the basic phase up to 1450°C, but the X-ray diffraction patterns for the 58.5AZG powder after 1150°C show M-ZrO_2, remaining up to 1450°C.

Hence, analysis of changes in the phase composition of the 90AZG and 58.5AZG powders during heat treatment indicates that temperature of the F-ZrO_2 → T-ZrO_2 phase transformation decreases from 850 to 700°C with a greater amount of the ZrO_2 solid solution in the ZTA composite. In addition, contrastingly to 90AZG, the 58.5AZG powder has no γ-Al_2O_3 phase, and the δ-Al_2O_3 → Θ-Al_2O_3 phase transition begins earlier. The M-ZrO_2 phase emerges in the 58.5AZG powder only at 1150°C and is retained in the heat treatment process up to 1450°C.

The sizes of primary Al_2O_3 and ZrO_2 particles in the 90AZG and 58.5AZG powders versus the heat treatment temperature are shown in Fig. 5.

When γ-Al_2O_3 forms from boehmite in the nanocrystalline 90AZG powder, primary Al_2O_3 particles become almost one third the original size (5 nm versus 15 nm). In the temperature range where both γ-Al_2O_3 and

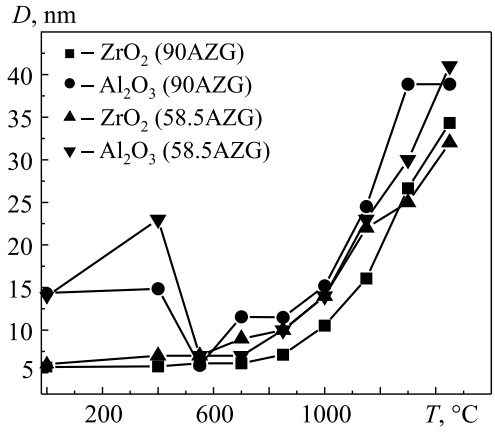

Fig. 5. Sizes of primary Al_2O_3 and ZrO_2 particles in the 90AZG and 58.5AZG powders versus the heat treatment temperature

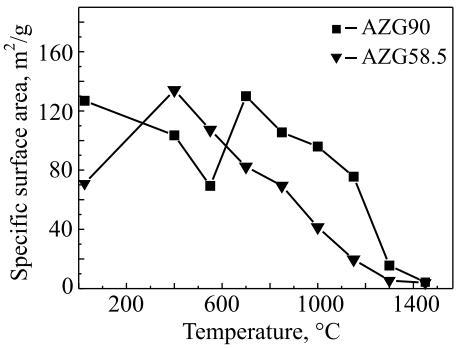

Fig. 6. Specific surface area of the nanocrystalline 90AZG and 58.5AZG powders versus the heat treatment temperature

δ-Al_2O_3 are found, the primary Al_2O_3 particles coarsen once again. The coarsening of primary Al_2O_3 particles in the 90AZG powder accelerates in the δ-Al_2O_3 → Θ-Al_2O_3 → α-Al_2O_3 phase transformation and, when it is finished, the particle sizes remain almost unchanged. The primary ZrO_2 particles of the 90AZG powder start coarsening after the F-ZrO_2 → T-ZrO_2 phase transformation finishes (Fig. 5).

With increasing content of the ZrO_2 solid solution in ZTA composites, the decomposition of boehmite involves a sharp variation in the sizes of primary particles (Fig. 5). After δ-Al_2O_3 emerges in the range 550–700°C, heat treatment of the 58.5AZG powder hardly causes the Al_2O_3 particles to coarsen. Note also that the sizes of F-ZrO_2 primary particles change insignificantly in the range 400–700°C. The δ-Al_2O_3 → Θ-Al_2O_3 → α-Al_2O_3 phase transformation involves an almost triple increase in the sizes of primary Al_2O_3 particles. Two temperature ranges (850–1150°C and 1150–1450°C) were found for ZrO_2: primary particles grow at different rates in these ranges (Fig. 5). According to XRD, the F-ZrO_2 → T-ZrO_2 phase transformation in the 58.5AZG powder finishes before 700°C and M-ZrO_2 traces appear after 1150°C. This variation in the sizes of primary ZrO_2 particles as a function of heat treatment temperature is due to M-ZrO_2 formed in the 58.5AZG powder.

Analysis of Fig. 6 shows that boehmite decomposition leads to abnormal dependence of the powder specific surface area on the heat treatment temperature: the specific surface area of the 90AZG powder reduces and that of the 58.5AZG powder reaches a maximum at 400°C and decreases when boehmite decomposes completely. In the process of further heat treatment involving phase transformations of Al_2O_3 and ZrO_2, the specific surface area of the 90AZG powder versus the heat treatment temperature reaches maxima and then reduces. The specific surface area of the 58.5AZG powder decreases almost monotonically to 1300°C. This process significantly slows down after α-Al_2O_3 is developed in the powders and they are sintered in the range 1300–1450°C (Fig. 6).

Figure 7 shows SEM data for the nanocrystalline 90AZG and 58.5AZG powders following heat treatment. Comparison of Figs. 2 and 7 implies that the powder morphology changes continuously. The agglomerates retain their shape, but the decomposition of boehmite and phase transformations of ZrO_2 and Al_2O_3 change the size distribution of the agglomerates. The AMIC (Automatic Microstructure Analyzer) software was used to process the powder morphology analysis data [29]. The image processing algorithm for quantifying the metallographic data relies on the Cavalieri–Aker–Glagolev principle [30].

Figure 8 shows the shape factors of the nanocrystalline 90AZG and 58.5AZG powders versus the heat treatment temperature. The shape factor of each powder indicates how much the actual particle shape deviates from a sphere. The paper [30] reports the following shape factors for a number of plane objects: 0.777 for a regular triangle, 0.886 for a square, 0.953 for a regular hexagon, and 1 for a circle. Note that agglomerates in the starting nanosized 90AZG and 58.5AZG powders are distributed in a similar way in terms of their shape factors (Fig. 8*a*, *b*). The powders contain a small number of agglomerates with low shape factors (0.35–0.50), being indicative of irregular agglomerates with a developed surface area. There are mainly agglomerates with a shape factor of 0.9, corresponding to multifaceted regular agglomerates (Fig. 8*a*, *b*). Agglomerates with a shape factor up to 0.5 amount

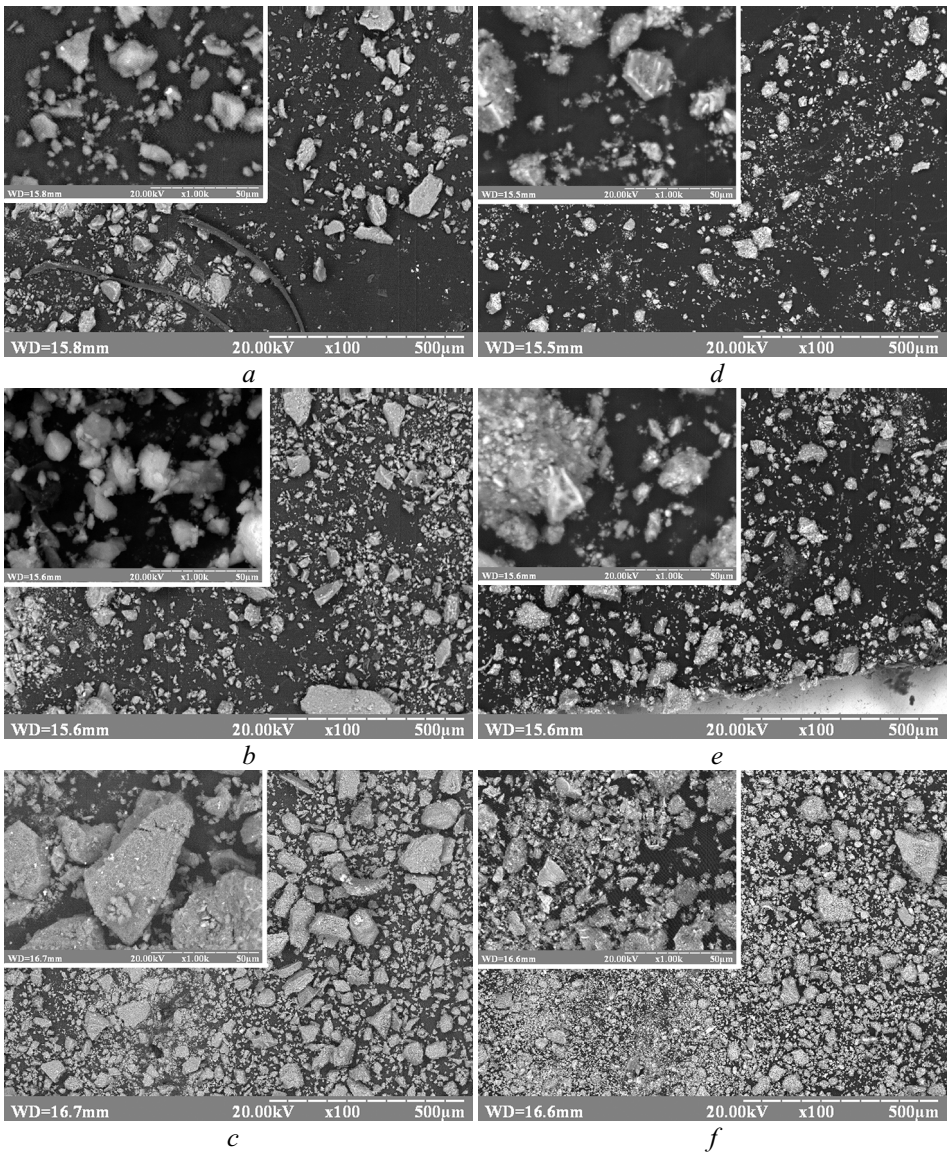

Fig. 7. SEM data for the nanocrystalline 90AZG and 58.5AZG powders following heat treatment at 550 (*a*, *d*), 850 (*b*, *e*), and 1450°C (*c*, *f*)

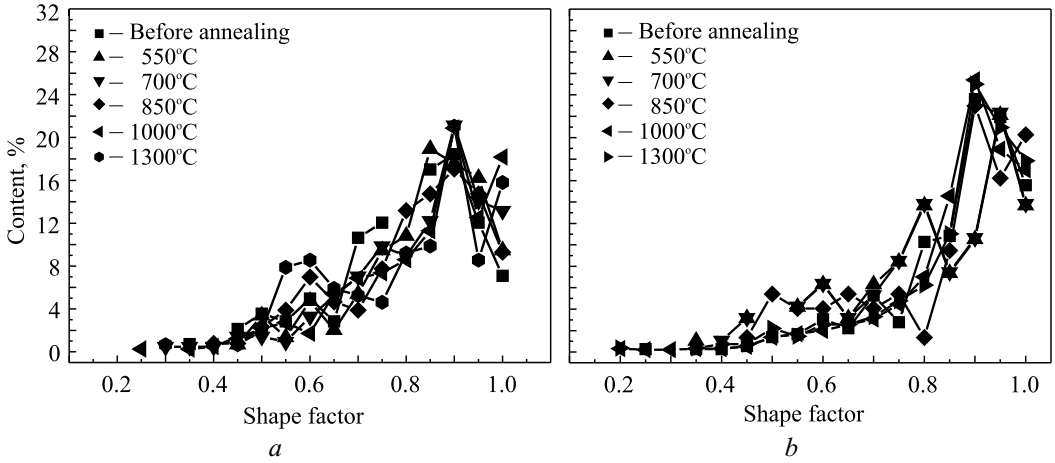

Fig. 8. Variation in the content of agglomerates with a specific shape factor in the 90AZG (*a*) and 58.5AZG (*b*) powders following heat treatment

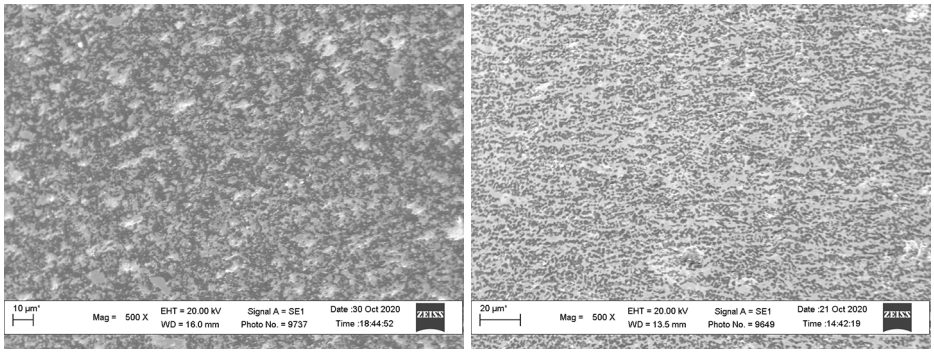

a *b*

Fig. 9. Microstructure of the 90AZG (*a*) and 58.5AZG (*b*) ZTA composites sintered at 1500°C

to no more than 4% in both powders, being indicative of regular agglomerates. The above distribution indicates that round agglomerates and multifaceted regular agglomerates are predominant in the nanocrystalline 90AZG and 58.5AZG powders.

The dependences showing the shape factors of the heat treated powders versus the heat treatment temperature are identical to those for the starting powders. Insignificant variations are due to the decomposition of boehmite, phase transformations of ZrO_2 and Al_2O_3, and sintering of loose powders (Fig. 8*a*, *b*). The results testify that the powders manifest a topochemical memory effect in the heat treatment process (Fig. 8*a*, *b*).

Pellet samples 2 cm in diameter and 0.5 cm in height were prepared by cold uniaxial pressing to study the mechanical properties of the composites produced from the hydrothermal 90AZG and 58.5AZG powders subjected to heat treatment at 850°C. The samples were sintered in air at 1500°C and held for 1.5 h at the sintering temperature. The relative density of the sintered samples varied between 0.95 and 0.97. The T-ZrO_2 and α-Al_2O_3 phases were found in the 90AZG samples after sintering at 1500°C and, besides the T-ZrO_2 and α-Al_2O_3 phases, M-ZrO_2 traces were identified in the 58.5AZG samples.

The 90AZG ZTA composite acquired a porous microstructure containing two phases, light and dark (Fig. 9*a*). The light phase is a ZrO_2 solid solution, while the dark phase consists of Al_2O_3. Fine particles of the ZrO_2 solid solution varying between 1 and 2 μm are quite uniformly distributed in the Al_2O_3 matrix with grains within 5 μm. Nevertheless, Fig. 9*a* shows that individual ZrO_2 grains can reach 3–5 μm.

The distribution of the light (ZrO_2) and dark (Al_2O_3) phases in the 58.5AZG composite (Fig. 9*b*) differs from that in the 90AZG ZTA composite. Figure 9*b* indicates that areas within 30 μm that contain ZrO_2 were formed by sintering at 1500°C in the 58.5AZG composite. The areas having Al_2O_3 grain accumulations at their boundaries are rounded and elongated. The homogeneous areas of the composite show directionally oriented Al_2O_3 grains. The ceramic composite is assumed to manifest a topological memory effect in this case. The 58.5AZG composite corresponds to the eutectic composition of the binary Al_2O_3–ZrO_2 system. This factor influences how the composite acquires its microstructure when sintered at 1500°C. The microhardness and Vickers hardness decrease and the critical fracture toughness factor increases with higher content of the ZrO_2 solid solution in the ZTA composite (Table 2).

TABLE 2. Mechanical Properties of the ZTA Composites

Properties	90AZG	58.5AZG
Microhardness, MPa	195	160
K_{Ic}, MPa · $m^{0.5}$	6	8
Vickers hardness, GPa	8.30	5.6

Greater consolidation of ZTA composites will improve their mechanical characteristics for the microstructural design of tool, structural, and functional materials with required properties.

CONCLUSIONS

Nanocrystalline powders in the Al_2O_3–ZrO_2 (Y_2O_3, CeO_2) system with low and high contents of the ZrO_2 solid solution, such as 90AZG and 58.5AZG, have been produced by hydrothermal synthesis in an alkaline environment.

Two phases form in both powders following hydrothermal synthesis: boehmite and low-temperature metastable F-ZrO_2. Heat treatment of the hydrothermal powders involves the decomposition of boehmite and phase transformations of Al_2O_3 and ZrO_2, depending on the content of the ZrO_2 solid solution in ZTA composites. The sequence of Al_2O_3 and ZrO_2 phase transformations in the 90AZG powder is as follows: γ-$Al_2O_3 \rightarrow \delta$-$Al_2O_3 \rightarrow$ $\rightarrow \Theta$-$Al_2O_3 \rightarrow \alpha$-$Al_2O_3$ and F-$ZrO_2 \rightarrow$ T-ZrO_2. The sequence of Al_2O_3 and ZrO_2 phase transformations in the 58.5AZG powder differs: δ-$Al_2O_3 \rightarrow \Theta$-$Al_2O_3 \rightarrow \alpha$-$Al_2O_3$ and F-$ZrO_2 \rightarrow$ T-$ZrO_2 \rightarrow$ T-ZrO_2 + M-ZrO_2.

With greater amount of the ZrO_2 solid solution in ZTA powders, temperature of the F-$ZrO_2 \rightarrow$ T-ZrO_2 phase transformation decreases by 150°C (from 850 to 700°C). In the range 1150–1450°C, the M-ZrO_2 content increases, no γ-Al_2O_3 is present, and incipient temperature of the δ-$Al_2O_3 \rightarrow \Theta$-$Al_2O_3$ phase transformation decreases (from 1150 to 1000°C).

'Soft' irregular multifaceted agglomerates consisting of primary particle agglomerates (to 1 μm) form in the 90AZG and 58.5AZG powders. They mainly differ by size: 5–15 μm agglomerates are predominant in the 90AZG powder and agglomerates ranging from 15 to 40 μm prevail in the 58.5AZG powder. The 90AZG and 58.5AZG powders remain nanocrystalline at all heat treatment stages in the range 400–1450°C, which makes the powders more active. The powder morphology changes continuously in terms of topology in the heat treatment process. Variations in the shape factors of agglomerates result from a topochemical memory effect. The nature of variations in the morphology and specific surface area in the heat treatment process indicates that the powders show increased sintering activity.

With greater ZrO_2 content, the microhardness of the ZTA composites decreases from 195 to 160 MPa, K_{Ic} increases from 6 to 8 MPa · $m^{0.5}$, and Vickers hardness reduces from 8.3 to 5.6 GPa.

Improvement in methods for the consolidation of ZTA composites will allow tool, structural, and functional materials with required properties to be produced.

ACKNOWLEDGEMENT

The authors are grateful to V.M. Pavlikov for the differential thermal analysis and to T.E. Babutina for determining the specific surface area of the powders.

REFERENCES

1. S. Rezaee, Kh. Ranjbar, and A.R. Kiasat, "Characterization and strengthening of porous alumina-20 wt.% zirconia ceramic composites," *Ceram. Int.*, **46**, No. 1, 893–902 (2020).
2. R.H.J. Hannink, P.M. Kelly, and B.C. Muddle, "Transformation toughening in zirconia-containing ceramics," *J. Am. Ceram. Soc*., **83**, No. 3, 461–487 (2000).
3. A.V. Shevchenko, A.K. Ruban, and E.V. Dudnik, "High-performance zirconium dioxide ceramics," *Ogneupory Tekh. Keram.*, No. 9, 2–8 (2000).
4. Yu.S. Karabasov (ed.), *New Materials* [in Russian], Mosk. Inst. Stali Splav., Moscow (2002), p. 736.
5. S.M. Olhero, Ib. Ganesh, P.M.C. Torres, F.J. Alves, and J.M.F. Ferreira, "Aqueous colloidal processing of ZTA composites," *J. Am. Ceram. Soc*., **92**, No. 1, 9–16 (2009).
6. S.R. Banik, I.M. Iqbal, R. Nath, L.J. Bora, B.K. Singh, N. Mandal, and M.R. Sankar, "State of the art on zirconia toughened alumina cutting tools," *Mater. Today: Proc.*, **18**, 2632–2641 (2019).

7. M.M. Basha, S.M. Basha, B.K. Singh, N. Mandal, and M.R. Sankar, "A review on synthesis of zirconia toughened alumina (ZTA) for cutting tool applications," *Mater. Today: Proc.*, **26**, Part 2, 534–541 (2020).
8. S. Huang, J. Binner, B. Vaidhyanathan, P. Brown, C. Hampson, and C. Spacie, "Development of nano zirconia toughened alumina for ceramic armor applications," *Adv. Ceram. Armor VII: Ceram. Eng. Sci. Proc.*, **32**, Issue 5, 103–115 (2011).
9. J. Chevalier and L. Gremillard, "Zirconia as a biomaterial," *Compr. Biomater. II*, **1**, 122–144 (2017).
10. R. Benzaid, J. Chevalier, M. Saadaoui, G. Fantozzi, M. Nawa, and L.A. Diaz, "Fracture toughness, strength and slow crack growth in a ceria stabilized zirconia-alumina nanocomposite for medical applications," *Biomaterials*, **29**, 3636–3641 (2008).
11. S. Tanaka, M. Takaba, Y. Ishiura, E. Kamimura, and K. Baba, "A 3-year follow-up of ceria stabilized zirconia/alumina nanocomposite (Ce-TZP/A) frameworks for fixed dental prostheses," *J. Prosthodont. Res.*, **59**, 55–61 (2015).
12. P. Sengupta, A. Bhattacharjee, and H.S. Maiti, "Zirconia: A unique multifunctional ceramic material," *Trans. Indian. Inst. Met.*, **72**, No. 8, 1981–1998 (2019).
13. S. De Bernardi-Martin, B.M. Moshtaghioun, D.G. Garcia, and A. Dominguez-Rodriguez, "Grain-boundary cation diffusion in ceria tetragonal zirconia determined by constant strain-rate deformation tests," *J. Eur. Ceram. Soc*., **34**, 4469–4472 (2014).
14. Y. Hao, C-K. Yang, and S.M. Haile, "Ceria–zirconia solid solutions ($Ce_{1-x}Zr_xO_{2-\delta}$, $x \le 0.2$) for solar thermochemical water splitting," *Thermodyn. Study, Chem. Mater.*, **26**, 6073–6082 (2014).
15. M. Kuhn, S.R. Bishop, J.L.M. Rupp, and H.L. Tuller, "Structural characterization and oxygen nonstoichiometry of ceria–zirconia ($Ce_{1-x}Zr_xO_{2-\delta}$) solid solutions," *Acta Mater.*, **61**, 4277–4285 (2013).
16. J. Chen, Z. Xie, W. Zeng, and W. Wu, "Toughening mechanisms of ZTA ceramics at cryogenic temperature (77 K)," *Ceram. Int.*, **43**, No. 4, 3970–3974 (2017).
17. J.-H. Ouyang, Y.-H. Ma, and A. Henniche, "Synthesis, densification and characterization of nanosized oxide ceramic powders with eutectic compositions by heating of alcohol–aqueous salt solutions," *J. Ceram. Sci. Technol.*, **8**, 81–90 (2017).
18. B.J. Oberste, J. Legouxu, and J. Gabriel, "Mechanical and thermal transport properties of suspension thermal sprayed alumina-zirconia composite coatings," *J. Therm. Spray Technol.*, **17**, Issue 1, 91–104 (2008).
19. F. Tarasi, M. Medraj, and A. Dolatabadi, "Phase formation and transformation in alumina/YSZ nanocomposite coating deposited by suspension plasma spray process," *J. Therm. Spray Technol.*, **19**, 787–795 (2010).
20. S.V. Veselov, N.S. Stukacheva, and R.I. Kuzmin, "Structure and mechanical properties of Al_2O_3–ZrO_2 ceramic materials," *Nauch. Vest. NGTU*, **65**, No. 4 207–217 (2016).
21. N.V. Sharova, N.A. Popova, and E.S. Lukin, "Effect of eutectic addition in the Al_2O_3–ZrO_2–Y_2O_3 system on the properties of corundum ceramics," *Usp. Khim. Khim. Tekhnol.*, **XXXI**, No. 3, 119–121 (2017).
22. V. Ponnilavan and S. Kannan, "Structural, morphological and mechanical characteristics on the role of excess ceria additions in zirconia toughened alumina systems," *J. Alloys Compd.*, **694**, 1073–1082 (2017).
23. Z.D.I. Sktani, N.A. Rejab, A.F.Z. Rosli, A. Arab, and Z.A. Ahmad, "Effects of La_2O_3 addition on microstructure development and physical properties of harder ZTA-CeO_2 composites with sustainable high fracture toughness," *J. Rare Earths* (2020), DOI: https://doi.org/10.1016/j.jre.2020.06.005.
24. Ah.Z.Ah. Azhar, S.H.M. Shawal, H. Manshor, A.M. Ali, N.A. Rejab, E.Ch. Abdullah, and Z.A. Ahmad, "The effects of CeO_2 addition on the physical and microstructural properties of ZTA-TiO_2 ceramics composite," *J. Alloys. Compd.*, **773**, 27–33 (2019).
25. P. Tana, Y. Yanga, Y. Suia, and Y. Jianga, "Influence of CeO_2 addition on the microstructure and mechanical properties of zirconia-toughened alumina (ZTA) composite prepared by spark plasma sintering," *Ceram. Int.*, **46**, Issue 6, 7510–7516 (2020).

26. N.K. Mitra, Supratim Das, S. Maitra, U. Sengupta, and A. Basumajumdar, "Effect of CeO_2 on the sintering behavior of zirconia–alumina composite," *Ceram. Int.*, **28**, 827–833 (2002).
27. M.Yu. Smyrnova-Zamkova and O.V. Dudnik, "Methods of producing starting nanocrystalline powders in the Al_2O_3–ZrO_2(Y_2O_3, CeO) system," in: *Current Issues of Materials Science: Collected Papers* [in Russian], Inst. Probl. Materialoved. NAN Ukrainy, Kyiv (2017), Issue 26, pp. 50–65.
28. M.Yu. Smyrnova-Zamkova, O.K. Ruban, O.I. Bykov, O.I. Khomenko, and O.V. Dudnik, "Synthesis and properties of a nanocrystalline eutectic powder in the Al_2O_3– ZrO_2(Y_2O_3, CeO_2) system," *Adhez. Raspl. Paika Mater.*, Issue 52, 35–44 (2019).
29. O.I. Khomenko and O.V. Khomenko, "Use of the AMIC software package for quantitative metallography," in: *Mathematical Models and Computer Experiments in Material Science: Collected Papers* [in Ukrainian], Inst. Probl. Materialoved. NAN Ukrainy, Kyiv (2014), Issue 16, pp. 35–42.
30. K.S. Chernyavskii, *Stereology in Metal Science* [in Russian], Metallurgiya, Moscow (1977), p. 280.